Materials Advances

ROYAL SOCIETY OF CHEMISTRY

PAPER

View Article Online
View Journal | View Issue



Cite this: *Mater. Adv.*, 2025, **6**, 4456

# Connectivity and twist: engineering high-performance green phosphorescent OLEDs using unipolar symmetric bicarbazole regioisomers†

Kalidass Kollimalaian, [a] Jia-Fan Wu,‡[b] Yu Hsuan Lin,‡[c] Ya-Hsin Cheng,[b] Premkumar Gnanasekaran,[c] Sudhakar Maddala, [a] Mandy M. Lee,[d] Shih-Sheng Sun, [d] Chih-Hao Chang, *[b] Yuan Jay Chang *[c] and Venkatakrishnan Parthasarathy *[a]

Received 6th October 2024,
Accepted 26th May 2025

DOI: 10.1039/d4ma01003e

rsc.li/materials-advances

Molecular structural differences by position can be crucial in developing promising materials for device applications. We synthesized four regioisomeric symmetric bicarbazoles (**BCzPh**) with distinct dihedral angle twists using oxidative C–C coupling or transition-metal catalyzed Suzuki coupling methods. The structural differences in connectivity manifested in fine-tuning of the photophysical, thermal, and electrochemical properties of the materials, as well as the device performance. Particularly, understanding the balance between the resonance and conjugation effects seems crucial for manipulation of triplet energy levels. Our findings indicate that bicarbazoles with greater twist angles exhibit larger singlet–triplet/HOMO–LUMO energy gaps, and improved power and luminance efficiencies, benefiting phosphorescent organic light-emitting diode (PhOLED) devices. The external quantum efficiencies of PhOLEDs were over 23.4% and 23.9% for **BCzPh**-based devices B and D, with device C reaching a maximum brightness of 203 490 cd $m^{-2}$, followed by device A at 96 953 cd $m^{-2}$. Notably, all **BCzPh** compounds served as excellent host materials, demonstrating stable, high-purity green-color emission in devices that turned on at voltages as low as 2.2 V.



## 1. Introduction

Phosphorescent OLEDs (PhOLEDs) have garnered immense attention due to their potential to achieve nearly 100% internal quantum efficiency (IQE) by efficiently harnessing both singlet and triplet excitons.[1,2] The development of high-triplet-energy organic host materials with suitable energy levels is crucial for ensuring optimal charge balance, exciton confinement, and efficient energy transfer to dopants.[3,4] While various molecular hosts, including bipolar (donor–acceptor) and non-polar systems, have been extensively explored for their structure–property relationships,[5–12] these studies have often lacked a systematic approach to molecular design and optimization.

Positional isomerism has recently emerged as a powerful yet underutilized strategy for fine-tuning the electronic and optical properties of organic semiconductors, thereby enhancing optoelectronic device performance.[5–19] Several studies with positional isomers have demonstrated that subtle variations in linkage positions can yield promising molecular candidates with high OLED efficiencies,[11,13–17] tunable solid-state packing,[20–22] tailored emission characteristics,[12,20,23] ultralong organic phosphorescence,[12,24–26] highly efficient perovskite solar cells,[18,19,27] *etc.* For instance, Poriel *et al.* demonstrated how variations in phenyl linkages (*ortho*, *meta*, and *para*) and steric congestion between spirobifluorene (SBF) units dictate the electrochemical and optical properties of regioisomeric SBF dimers, revealing distinct optical and electronic characteristics for each positional isomer.[6,7,9,28,29] These studies underscore the profound impact of regioisomeric control on molecular properties, reinforcing the need for systematic investigations into positional effects across different molecular scaffolds for developing efficient devices.

Among various organic semiconductors, carbazole-based host materials have gained prominence due to their high triplet energy ($E_T$ > 2.95 eV), efficient hole transport, superior charge carrier mobility, and exceptional thermal, morphological, chemical, and photochemical stability.[30–38] Their synthetic

[a] *Department of Chemistry, Indian Institute of Technology Madras, Chennai-600 036, Tamil Nadu, India. E-mail: pvenkat@zmail.iitm.ac.in*
[b] *Department of Electrical Engineering, Yuan Ze University, Chung-Li, 32003, Taiwan. E-mail: chc@saturn.yzu.edu.tw*
[c] *Department of Chemistry, Tunghai University, No. 1727, Sec. 4, Taiwan Boulevard, Xitun District, Taichung 40704, Taiwan. E-mail: jaychang@thu.edu.tw*
[d] *Institute of Chemistry, Academia Sinica, Taipei 115201, Taiwan*

† Electronic supplementary information (ESI) available. CCDC 2361782–2361784. For ESI and crystallographic data in CIF or other electronic format see DOI: https://doi.org/10.1039/d4ma01003e

‡ Equal contribution first author.

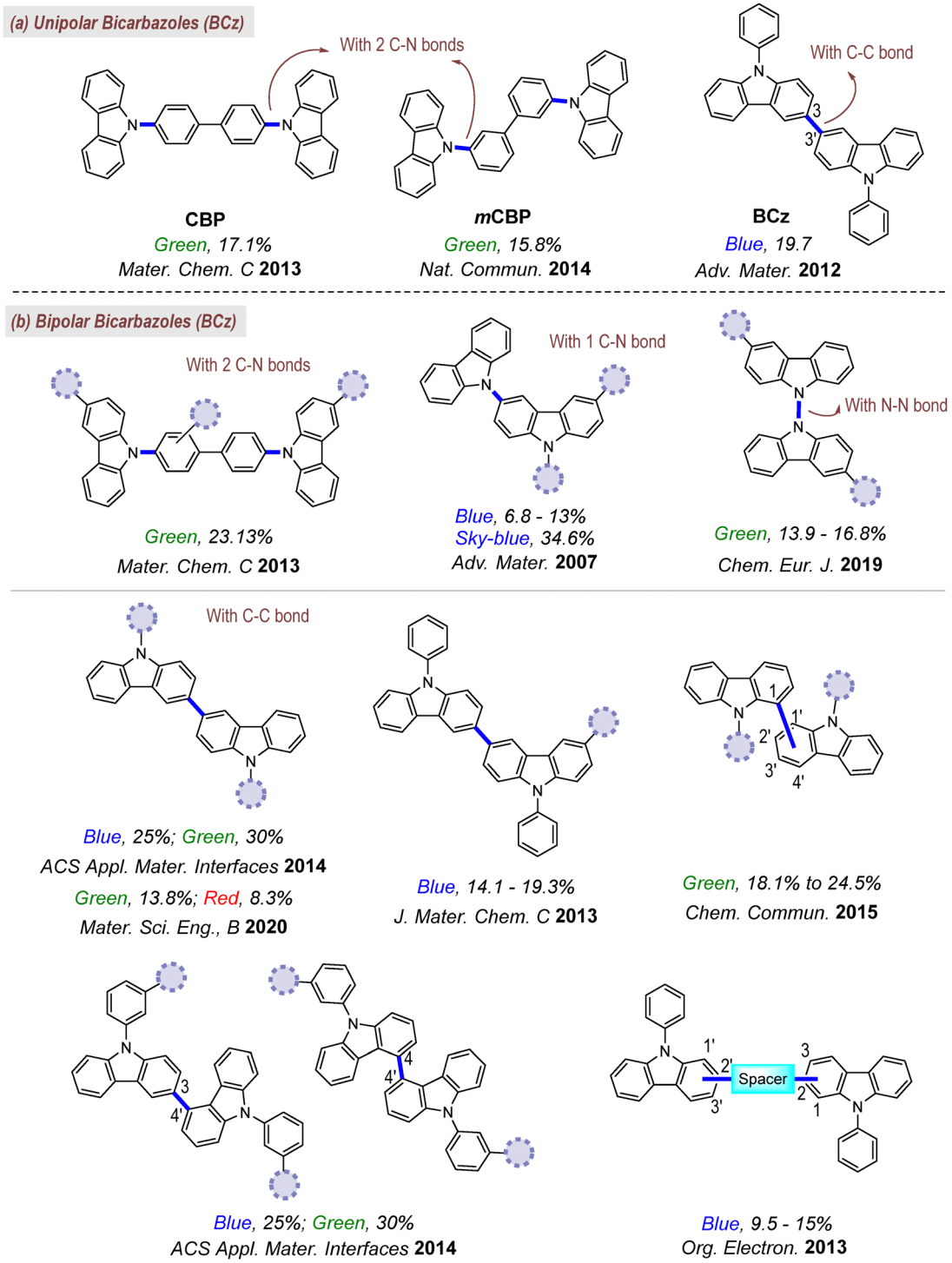


Fig. 1 Unipolar and bipolar bicarbazole (BCz) host designs reported previously.

versatility, stable radical cations, and favourable electronic properties further enhance their potential in optoelectronic applications.[3,4,39–45] Although extensive studies have explored carbazole functionalization at the 2,7- and 3,6-positions, as well as at the nitrogen atom, systematic studies correlating the structure and properties of bicarbazole (BCz) derivatives—comprising two carbazole units linked *via* C–C or C–N bonds—remain limited (Fig. 1).[3,39,46–48] These bicarbazole architectures, depending on the connectivity of two carbazole units, provide a versatile platform for optimizing charge transport and triplet energy levels. Notably, 3,3′-bicarbazole (**BCz**, Fig. 1a) exhibits a small singlet–triplet energy gap ($\Delta E_{ST}$ = 0.46 eV) and a high triplet energy ($E_T$ = 2.8 eV),[49] making it a promising candidate for PhOLED applications. While **CBP**

(4,4′-bis(9-carbazolyl)-2,2′-biphenyl, $E_T$ = 2.6 eV; Fig. 1a) is widely employed as a green phosphor host,[50–52] its relatively low $E_T$ can lead to reverse energy transfer from blue-emitting guests to hosts. In contrast, ***m*CP** (1,3-bis(9-carbazolyl)-benzene, $E_T \approx 3.00$ eV; Fig. 1a) offers a higher $E_T$, making it more suitable for blue PhOLEDs.[3,53–60] Diverse dipolar structural modifications of **BCz**, ***m*CP** and **CBP** through (i) substituents on nitrogen,[61–63] (ii) reactive carbon center(s),[62–64] and (iii) connectivity (symmetrical/unsymmetrical) differences and spacer linkages[47,62,65–69] were explored, besides N–N bridged bicarbazoles reported recently (Fig. 1b).[48,70,71] Despite these advances, regioisomeric effects in unipolar symmetric bicarbazoles remain largely unexplored, particularly in relation to charge transport and exciton management.

In this work, we systematically investigate four regioisomeric bicarbazole derivatives—**1,1′-BCzPh**, **2,2′-BCzPh**, **3,3′-BCzPh**, and **4,4′-BCzPh**—where C–C bonds symmetrically link two carbazole units, leading to distinct molecular architectures (Chart 1). Although these isomers share the same molecular formula, variations in connectivity induce varying degrees of dihedral angles, π-conjugation, and resonance effects. Notably, **3,3′-BCzPh** exhibits strong resonance due to *para–para* nitrogen connectivity, while **2,2′-BCzPh**, with *meta–meta* nitrogen positioning, limits conjugation. The steric constraints in **1,1′-BCzPh** and **4,4′-BCzPh** result in greater twist angles, restricting extended conjugation and modifying their electronic properties. Moreover, **1,1′-BCzPh** alone instils through-space conjugation between the *N*-phenyl and carbazole rings. These structural differences significantly influence electronic structure/properties, mesomeric effects, and triplet energy levels, making them ideal candidates for systematic study.[72–75] We present a comprehensive structure–property analysis, integrating experimental and DFT studies to correlate molecular conformation with electronic, thermal, and photophysical properties. Furthermore, we evaluate their performance as host materials in green PhOLEDs, where notable differences emerge in luminescence and external quantum efficiencies (EQE). Remarkably, π-extended **3,3′-BCzPh** exhibited the highest luminescence (203 490 cd $m^{-2}$), while **2,2′-BCzPh** and **4,4′-BCzPh** achieved high EQEs of 23.4% and 23.9%, respectively—outperforming other isomers and conventional CBP-based hosts. These findings underscore the critical role of regioisomerism in tailoring material properties and advancing next-generation PhOLED design and applications.

## 2. Results and discussion

### 2.1. Synthesis and characterization

The positional isomers of bicarbazole (**1,1′-BCzPh**, **2,2′-BCzPh**, **3,3′-BCzPh**, and **4,4′-BCzPh**, Chart 1) were synthesized from their respective carbazole derivatives (please refer to pages S4–S6, ESI†). In particular, **3,3′-BCzPh** was synthesized from *N*-phenylcarbazole using our metal-free oxidative coupling reaction.[74,75] The other regioisomers—**1,1′-BCzPh**, **2,2′-BCzPh**, and **4,4′-BCzPh**—were synthesized starting from the corresponding bromocarbazole derivatives *via* a transition metal-catalyzed Suzuki cross-coupling reaction.[76] The synthesis of bicarbazoles typically involves the following steps: (i) *N*-arylation of 9*H*-carbazole using a copper catalyst,[72,73,77] (ii) borylation of bromocarbazole with a boronate ester reagent in the presence of palladium or *via* lithium–halogen exchange,[72,73] and (iii) Suzuki coupling between the appropriate bromocarbazole and carbazole boronate ester using a palladium catalyst. The synthesized symmetric bicarbazole isomers (BCz) were thoroughly characterized by spectroscopic (NMR and IR) and spectrometric (HRMS) analyses (Fig. S1–S3 and pages S3–S10, ESI†). Their structures were further confirmed by X-ray crystallography (Fig. S4–S6 and pages S11–S14, ESI†).

### 2.2. Structural properties

The X-ray structure analysis of **1,1′-BCzPh** (CCDC 2361782, triclinic, $P\bar{1}$; $Z$ = 2; Fig. 2a and Fig. S4, Table S1, ESI†) and **4,4′-BCzPh** (CCDC 2361783, orthorhombic, *Pbca*; $Z$ = 8; Fig. 2d

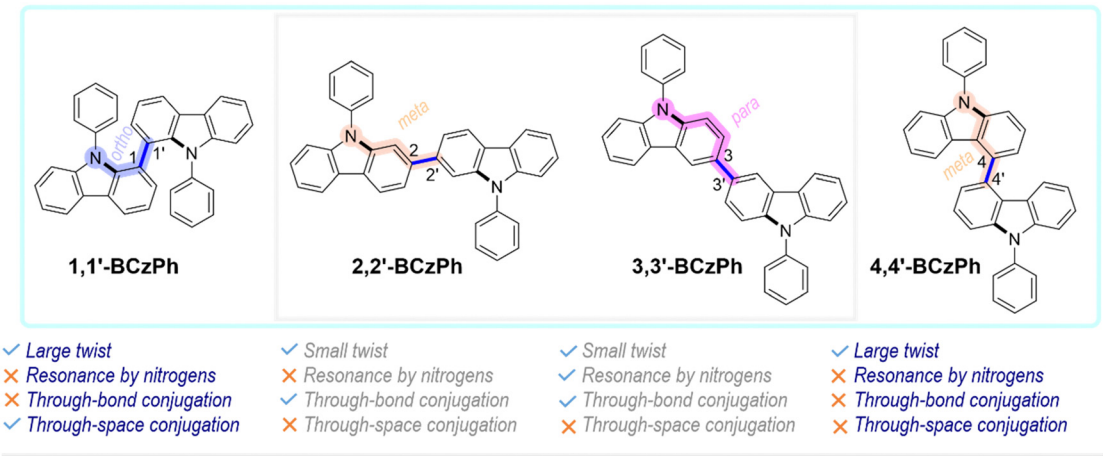


Chart 1 Regioisomeric symmetric bicarbazole (**BCzPh**) emissive host materials investigated for PhOLED applications in this report and their molecular features. The *ortho*, *meta* and *para* relationships between the C–C and C–N bonds are highlighted.

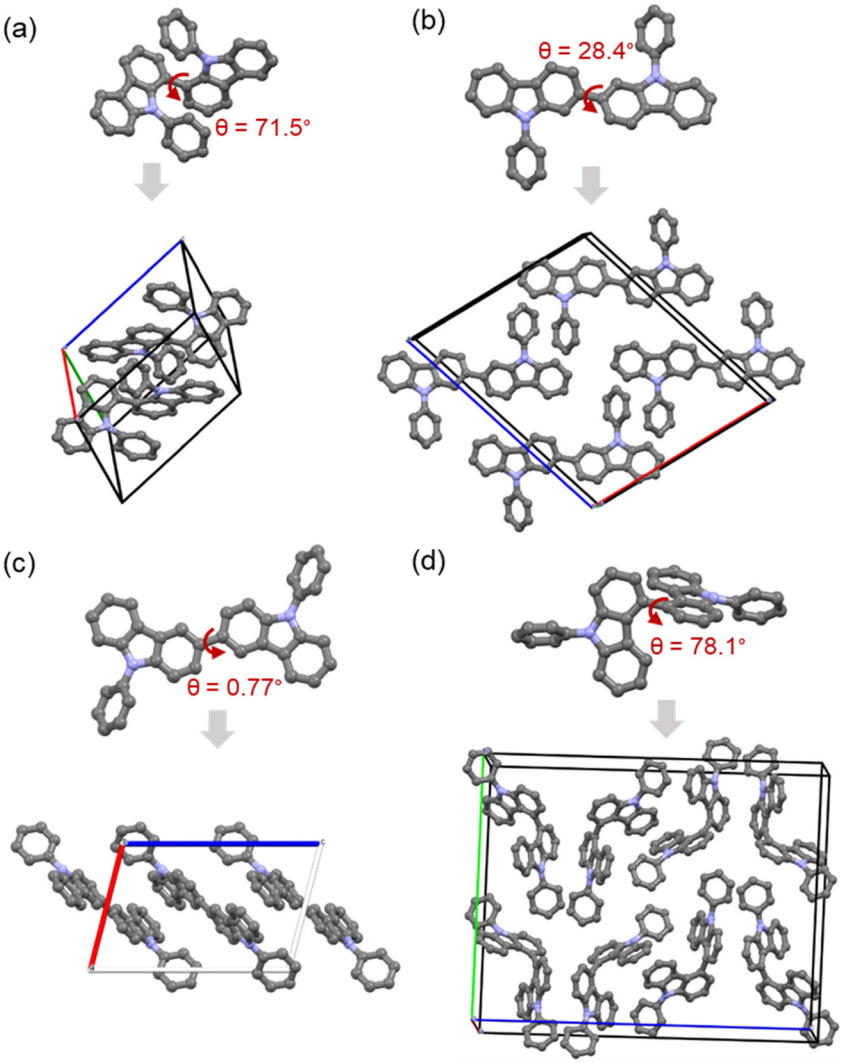


Fig. 2 The X-ray molecular structure (top row) and unit cell packing diagram (bottom row) of (a) **1,1′-BCzPh**, (b) **2,2′-BCzPh**, (c) **3,3′-BCzPh**,[55] and (d) **4,4′-BCzPh**. The dihedral angle ($\theta$, °) between the carbazole planes is indicated and the hydrogen atoms are removed for clarity.

and Fig. S6, Table S3, ESI†), revealed a non-planar, highly twisted geometry, in contrast to **2,2′-BCzPh** (CCDC 2361784, monoclinic, $P21/c$; $Z = 4$; Fig. 2b and Fig. S5, Table S2, ESI†) and **3,3′-BCzPh** (CCDC 1579239; Fig. 2c),[78] which likely results from greater steric repulsion between the *N*-aryl and carbazole rings in **1,1′-BCzPh**, and between the carbazole rings in **4,4′-BCzPh**, compared to the steric hindrance caused by hydrogens in **2,2′-BCzPh** and **3,3′-BCzPh**. Consequently, the dihedral angles ($\theta$) between the mean planes of the two carbazole rings were found to follow the order: 78.1° > 71.5° > 28.4° for **4,4′-BCzPh**, **1,1′-BCzPh**, and **2,2′-BCzPh**, respectively (Fig. 2). This twist trend is comparable to analogous spirobiflorene (SBF) dimers.[6,7,9,28,29] Besides, the new C–C bond length between the two carbazole rings in **BCzPh**s was measured to be *ca.* 1.486 Å, 1.490 Å, 1.496 Å for **1,1′-BCzPh**, **2,2′-BCzPh**, and **4,4′-BCzPh**, respectively. Previous report[74–78] has measured a torsion angle and C–C bond length of 0.77° and 1.491 Å, respectively, for **3,3′-BCzPh**. It is worth noting that substituents can significantly modify these solid-state structural parameters.[74,78] However, the C–C bond length measures suggest varying degrees of resonance in these systems, depending on their connectivity (steric inhibition of resonance), which aligns with the observed twist trend. Molecular packing analyses of the highly twisted **1,1′-BCzPh**, **4,4′-BCzPh**, and the relatively planar **2,2′-BCzPh** reveal that their solid-state arrangement is primarily driven by weak C–H···π or/and π–π stacking interactions. Both **2,2′-BCzPh** and **3,3′-BCzPh** exhibited staggered arrangements of (bi)carbazoles, with the **2,2′-BCzPh** stacking face-to-face in the same direction, while **3,3′-BCzPh** adopted a slip-stacked arrangement in opposite directions.[78] These highly planar structures and such packing configurations are advantageous for improving thermal stability and facilitating charge transport. In contrast, **1,1′-BCzPh** and **4,4′-BCzPh** lacked continuous carbazole–carbazole interactions, resulting in looser packing arrangements. Such twisted aryl systems are of great interest in inducing an amorphous character, which is crucial for

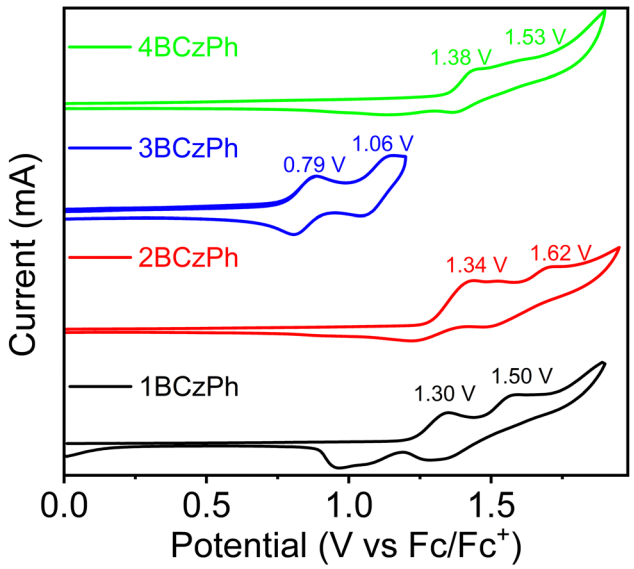


Fig. 3 Cyclic voltammograms of **BCzPh**s (1.0 mM) recorded in dichloromethane using $TBAPF_6$ (0.1 M) as the supporting electrolyte.

generating morphologically stable, pin-hole-free thin films during OLED fabrication, enhancing efficient recombination and device stability.[79,80] In contrast, more planar carbazole structures may function as efficient charge-transport systems.

### 2.3. Electrochemical properties

To understand the redox behavior, the cyclic voltammograms of the **BCz**s were recorded in dichloromethane solution (1.0 mM) using tetrabutylammonium hexafluorophosphate as the supporting electrolyte (Fig. 3 and Fig. S7, pages S15 and S16, ESI†). The **BCz**s display multiple (more than one electron) oxidation potentials, which are ascribed to the oxidation of two carbazole moieties connected distinctly. Their first oxidation potential increases in the order: **3,3′-BCzPh** < **1,1′-BCzPh** < **2,2′-BCzPh** < **4,4′-BCzPh**, indicating the influence of conjugation/mesomerism and variations in twist angles across these systems (Fig. 3 and Fig. S7, ESI†); mesomeric effects appear to dominate over π-conjugation in this context, highlighting the electron-rich nature of bicarbazole. The highest occupied molecular orbital (HOMO) energy levels (eV) of the **BCzPh**s were calculated from the onset oxidation potentials ($E_{OX}$) derived from differential pulse voltammograms (DPV), using the relation $E_{HOMO} = E_{OX} + 4.8$ eV against $Fc/Fc^+$. The lowest unoccupied molecular orbital (LUMO) energy values (eV) were obtained from the optical energy gap values ($E_g$, solution) and the corresponding HOMO energy values, using $E_{LUMO} = E_{HOMO} + E_g$ (in eV). The oxidation and reduction onset values, along with the corresponding HOMO (−5.45 eV to 5.64 eV) and LUMO (−2.32 eV to −2.18 eV) energy values, are summarized in Table 1 and Table S4 (ESI†). Notably, **3,3′-BCzPh**[63,78] and **2,2′-BCzPh** exhibit elevated HOMO energy levels compared to twisted **1,1′-BCzPh** and **4,4′-BCzPh**, likely due to extended π-conjugation and resonance in the former and steric inhibition of the same effects in the latter due to twisting. The HOMO energy level in **4,4′-BCzPh**, closely resembling that of simple *N*-phenylcarbazole (−5.64 eV),[78] suggests a lack of significant resonance and conjugation effects. This similarity implies that the extended electronic communication between the carbazole units is hindered, resulting in limited conjugation across the molecule. Overall, the HOMO energy values (−5.45 eV to −5.64 eV) observed for these bicarbazoles are comparable to that of CDBP[80] and CBP,[81] however lower than SBF dimers picturing nitrogen's role here.[6,7,9,28,29]

### 2.4. Thermal properties

To evaluate the functional utility of **BCzPh**s in PhOLED applications, their thermal stabilities were assessed through thermogravimetry (TGA) and differential scanning calorimetry (DSC) under a nitrogen gas atmosphere. The scans (Fig. 4 and Fig. S8, pages S16 and S17, ESI†) and data in Table 1 reveal that all **BCzPh**s exhibit high thermal stabilities, with decomposition temperatures ($T_d$ at 5% weight loss) exceeding 280 °C. Specifically, **2,2′-BCzPh** has a $T_d$ of 329 °C, higher than **4,4′-BCzPh** (291 °C) and **1,1′-BCzPh** (281 °C). This is probably linked to the relatively planar molecular structure of **2,2′-BCzPh** and **3,3′-BCzPh**, which promotes closer packing in the solid state. Fortunately, the thermal decomposition temperature of these **BCzPh** compounds align with their twist angle: the smaller the twist angle, the higher the thermal decomposition, and *vice versa*. Notably, the thermal stability of **BCzPh**s is comparable to that of other bicarbazole-based derivatives (***o*CBP**,[82] **BCz1**, **BCz2**, and **BCz3**[83]) reported previously in the literature. The high thermal stability is attributed to the bicarbazole core, which increases the overall molecular size. Furthermore, the complete mass loss beyond $T_d$, with no residual material,

Table 1 Optical, electrochemical and thermal characteristics of **BCzPh**s

| Molecule | Wavelength[a] (nm) | | | $\varphi_f$[d] (%) | $E_g$[b] (eV) | $E_{HOMO}$[c] (eV) | $E_{LUMO}$[c] (eV) | $T_d/T_m$[e] (°C) |
|---|---|---|---|---|---|---|---|---|
| | $\lambda_{onset}$ | $\lambda_{abs}$ | $\lambda_{em}$ | | | | | |
| **1,1′-BCzPh** | 366 | 332, 347 | 363 | 60 | 3.39 | −5.56 | −2.22 | 281/— |
| **2,2′-BCzPh** | 378 | 325, 349 | 390 | 76 | 3.28 | −5.60 | −2.32 | 329/234 |
| **3,3′-BCzPh**[75] | 379 | 310, 361 | 406 | 21 | 3.27 | −5.45 | −2.18 | 366/205 |
| **4,4′-BCzPh** | 373 | 330, 344 | 382 | 59 | 3.32 | −5.64 | −2.32 | 291/204 |

[a] Measured in dichloromethane solution at room temperature. [b] $E_g$, the optical energy gap is estimated from the threshold of the UV-vis absorption spectra using the relationship, $E_g = 1240/\lambda_{onset}$. [c] HOMO and LUMO energy levels are calculated from the onset of the first oxidation potential and the optical energy gap from the absorption spectra. [d] Quantum yield was measured in dichloromethane solution at room temperature with the reference of 9,10-diphenylanthracene. [e] $T_d$: decomposition temperature, $T_m$: melting point.

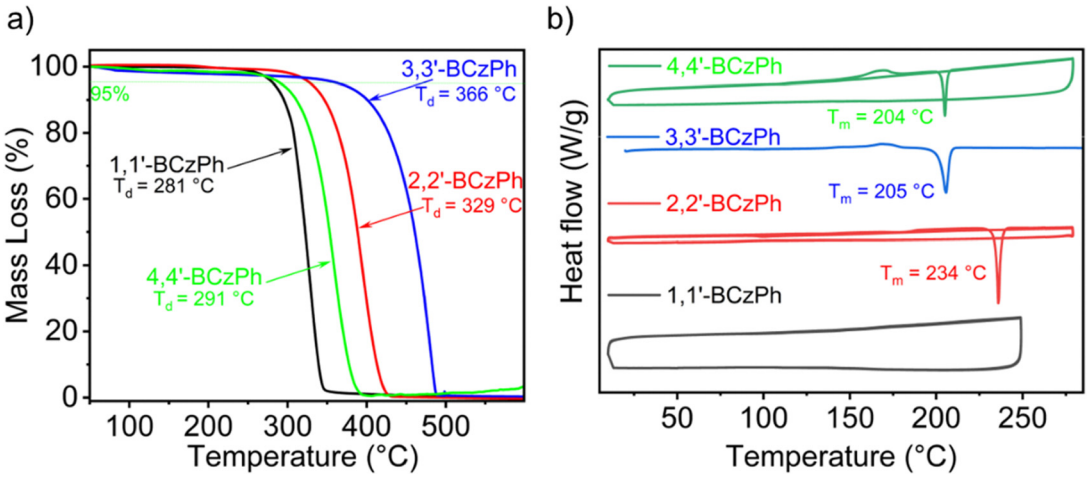


Fig. 4 (a) Thermal stability curves of the **BCzPh**s, recorded under a nitrogen gas atmosphere at a heating rate of 20 °C $min^{-1}$. (b) DSC traces of the heating and cooling cycles of **BCzPh**s under nitrogen gas atmosphere at a scan rate of 10 °C $min^{-1}$.

suggests that **BCzPh**s are promising candidates for fabricating devices under the vacuum-deposition method.

The DSC scans for most **BCzPh**s (Fig. 4) reveal a sharp endothermic melting transition ($T_m$) in the first heating cycle, except for **1,1′-BCzPh**, which showed no thermal transitions (up to 250 °C). Specifically, a melting transition was observed for **2,2′-BCzPh** at 234 °C and **4,4′-BCzPh** at 204 °C, alongside glass transitions ($T_g$) at *ca.* 175 and 160 °C, respectively (Fig. S8, ESI†). These $T_g$ values are significantly higher than the simple unipolar bicarbazole (C–N or C–C based) systems known in the literature[63,81–83] In comparison, previously reported **3,3′-BCzPh** exhibits a $T_d$ of 366 °C and $T_m$ of 205 °C, higher than the less-twisted counterpart **2,2′-BCzPh**.[63,75] The good thermal and amorphous properties of **BCzPh**s suggest they can offer enhanced morphological stability and uniform film-forming ability during vacuum deposition, making them suitable for device fabrication.

### 2.5. Optical properties in solution

The optical properties of isomeric **1,1′-BCzPh**, **2,2′-BCzPh**, **3,3′-BCzPh**, and **4,4′-BCzPh** were evaluated using UV-vis absorption and fluorescence spectroscopy in dilute dichloromethane solutions (*ca.* $10^{-5}$ M) at room temperature (Fig. 5 and Fig. S9, pages S17–S19, ESI†). The summarized results of all **BCzPh**s are gathered in Table 1 and Table S5 (ESI†). The **BCzPh**s revealed absorption bands tailing near the visible region up to *ca.* 380 nm, in contrast to simple carbazole (Cz).[25,84] The red-shifted absorption in **BCzPh**s, when compared to simple Cz, is attributed to extended π-conjugation resulting from the establishment of a new C–C bond between the two carbazole rings. The absorption spectral profile for the twisted **1,1′-BCzPh** and **4,4′-BCzPh** is similar, exhibiting clear vibronic bands, likely due to sterically restricted carbazole rotations. However, **2,2′-BCzPh** showed broader absorption bands with no vibronic features and a red-shift relative to **3,3′-BCzPh**. The optical

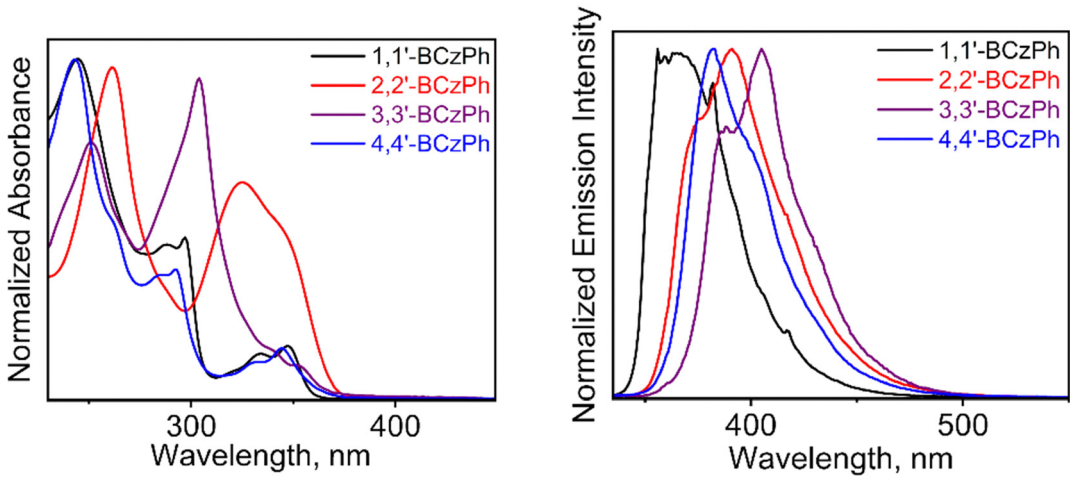


Fig. 5 Normalized UV-vis absorption (left) and emission (right) spectra of isomeric **BCzPh**s in dichloromethane (*ca.* $10^{-5}$ M).

energy gap ($E_g$) for **BCzPh**s, estimated from the onset of the absorption spectrum, ranged from 3.27 to 3.39 eV, which is smaller than that of analogous SBF dimers, emphasizing the resonance contribution of nitrogen atoms.[6,7,9,28,29] The highly twisted **1,1′-BCzPh** exhibited the largest energy gap, followed by the relatively less twisted isomers (*i.e.*, **4,4′-BCzPh** > **2,2′-BCzPh** > **3,3′-BCzPh**). Supportively, this trend in $E_g$ values is comparable to the theoretically derived ones; the electron density in the HOMO and LUMO was localized on the bicarbazole unit (Fig. S10 and Table S6, page S20, ESI†).

The emission spectra of **BCzPh**s (recorded at $\lambda_{exc}$ = 325 nm) presented characteristic vibronic patterns, typical of Cz, ranging from 350 to 450 nm.[25,84] Both **3,3′-BCzPh** and **2,2′-BCzPh** exhibited a red-shifted emission maxima compared to their regioisomeric counterparts **1,1′-BCzPh** and **4,4′-BCzPh**, respectively (Fig. 5, Table 1 and Fig. S9, Table S5, ESI†). In other words, the more planar BCz structures displayed emission near the visible region, while the twisted structures emitted in the UV region. The fluorescence quantum yields ($\phi_f$) measured in dichloromethane were in the range *ca.* 0.21–0.76 (Table 1 and Table S5, ESI†), with **2,2′-BCzPh** exhibiting the highest value (0.76). The severe steric interactions between carbazole planes in the twisted BCz structures likely increase overall rigidity, promoting radiative energy loss and resulting in high $\phi_f$s, as seen in **1,1′-BCzPh** and **4,4′-BCzPh** ($\phi_f$, *ca.* 0.60). In sharp contrast, the relatively less-twisted **3,3′-BCzPh** and **2,2′-BCzPh** likely permit free-rotation along the bridging C–C bonds, facilitating non-radiative decay and reducing their PLQYs. Interestingly, **2,2′-BCzPh** exhibits a *ca.* 3-fold increase in PLQY compared to **3,3′-BCzPh**, though the origin of this difference remains unclear. However, it may be discerned from the fact that the increment in PLQY (up to 62%) of **3,3′-BCzPh** when mixed with FIrpic dopant emitter, suggesting a possible non-radiative decay pathway in **3,3′-BCzPh**.[63] The optical properties of **BCzPh**s are consistent with those reported for **BCz** analogs.[53,81]

### 2.6. Photophysical properties in thin films

To replicate device-like conditions, the fluorescence and phosphorescence emission spectra were also examined in the thin-film state (*ca.* 60 nm) and in 77 K glassy matrices, respectively. The complete spectrum and associated data are presented in Fig. 6 and Table 2, respectively. When comparing the fluorescence spectrum of all synthesized compounds, it becomes clear that the **1,1′-BCzPh** film displays apparent vibronic features and a broader spectral profile, resembling the solution phase behavior. The full-width at half-maximum (FWHM) values for **1,1′-BCzPh**, **2,2′-BCzPh**, **3,3′-BCzPh**, and **4,4′-BCzPh** were estimated as 73, 53, 48, and 42 nm, respectively. The positioning of the two carbazole entities in **BCzPh**s significantly impacts their spectral profiles in both solution and film phases. The increased molecular symmetry and restricted molecular motion

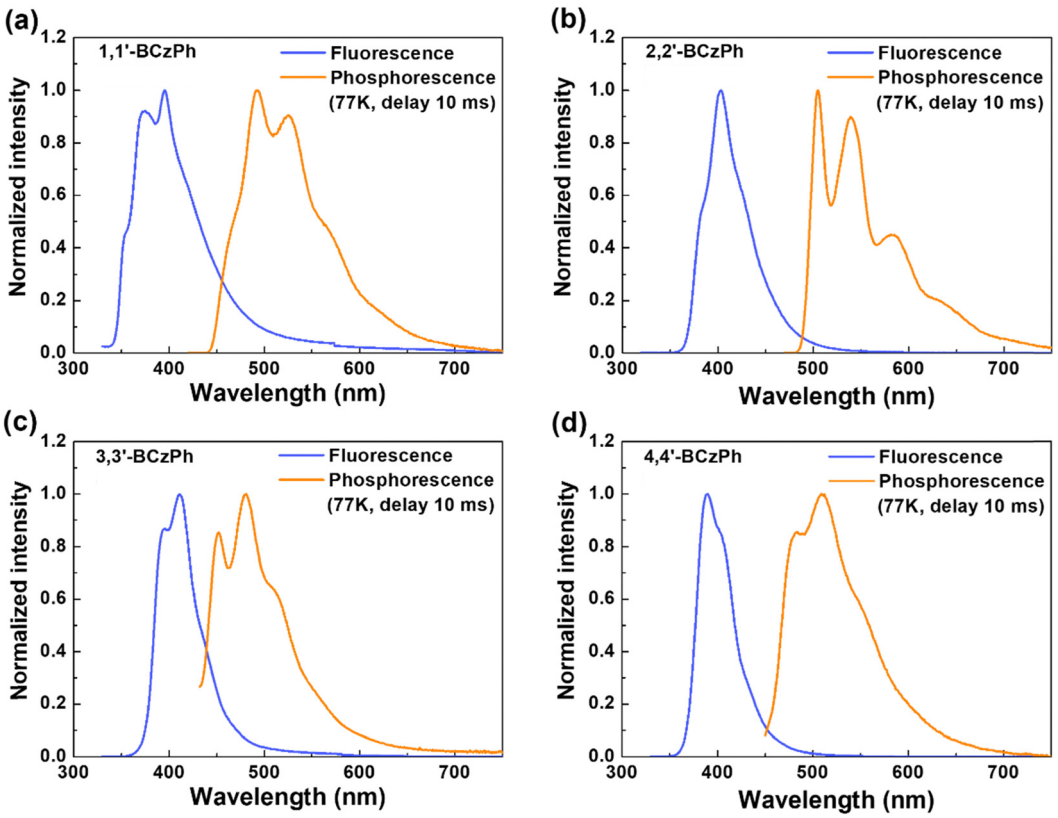


Fig. 6 Fluorescence (blue line, thin-film) and phosphorescence (orange line, in 2-MeTHF at 77 K) spectra of (a) **1,1′-BCzPh**; (b) **2,2′-BCzPh**; (c) **3,3′-BCzPh**; and (d) **4,4′-BCzPh**.

Table 2 Photophysical properties of **BCzPh**s

| Molecule | Fluorescence[a] $\lambda_{peak}$ (nm) | Phosphorescence[b] $\lambda_{peak}$ (nm) | $S_1$[c] (eV) | $T_1$[d] (eV) |
|---|---|---|---|---|
| **1,1′-BCzPh** | 353 (sh), 374, 395, 422 (sh) | 493, 525, 564 (sh) | 3.46 | 2.78 |
| **2,2′-BCzPh** | 382 (sh), 403, 426 (sh) | 505, 540, 583, 635 (sh) | 3.27 | 2.54 |
| **3,3′-BCzPh** | 395, 411, 433 (sh) | 451, 481, 510 (sh) | 3.36 | 2.87[63] |
| **4,4′-BCzPh** | 390, 403 (sh) | 583, 509, 548 (sh) | 3.33 | 2.73 |

[a] Fluorescence spectrum measured in neat films. [b] Phosphorescence spectrum measured in 2-MeTHF at 77 K. [c] Estimated from the fluorescence onset. [d] Estimated from the phosphorescence onset.

in **1,1′-BCzPh** probably contribute to clear vibronic features, reflecting enhanced rigidity.

The singlet energies ($S_1$) of the thin film samples did not fully match the calculated values derived from solution, which might result from the molecular packing effects and film morphology. Similarly, the triplet energies ($T_1$), determined from the onset of the phosphorescence spectrum, were found to be 2.78, 2.54, 2.87,[63] and 2.73 eV for **1,1′-BCzPh**, **2,2′-BCzPh**, **3,3′-BCzPh**, and **4,4′-BCzPh**, respectively. Although the more twisted **BCzPh** isomers (**1,1′-BCzPh** and **4,4′-BCzPh**) generally exhibited higher triplet and singlet energy levels, **3,3′-BCzPh** surprisingly exhibited the highest triplet energy in the series. This suggests that factors beyond molecular twisting, such as enhanced resonance effects, significantly contribute to the elevation of excited-state energy levels. Resonance and conjugation effects were both found to effectively elevate the singlet and triplet energy levels in **3,3′-BCzPh**, likely due to improved π-orbital overlap and charge delocalization. On the other hand, **2,2′-BCzPh**, which primarily benefits from conjugation but lacks substantial resonance stabilization, showed the lowest energy levels among the four isomers. The $T_1$ energy values of these isomers are comparable to unipolar bicarbazoles like ***m*CP**,[63] **CBP**,[81] or ***o*CDBP**,[82] although lower than 3-(9-carbazolyl)carbazoles[83] and SBF isomers.[6,7,9,28,29] Because efficient energy transfer in green phosphorescent OLEDs requires host materials with triplet energy levels typically above 2.5 eV, these results indicate that triplet energy levels can be effectively fine-tuned by engineering the twist angles *via* C–C coupling (in contrast to C–N coupling), which significantly impacts the molecular conformation and π–π interactions. Therefore, the BCz-based compounds investigated here demonstrate strong potential as host materials for green phosphorescent emitters.

### 2.7. Film morphology and carrier transport properties

We conducted the atomic force microscopy (AFM) measurements of the thin film samples fabricated on the glass substrate to assess whether the twisted aryl system could form amorphous, morphologically stable, and pinhole-free films for OLED applications. The results indicated that all four samples using synthesized **BCzPh**-based compounds could exhibit smooth morphologies, as shown in Fig. S11 (ESI†). The average roughness values, ranging from 1 to 2 nm, suggest that these materials have the potential to serve as ideal host materials.

The charge mobility of host materials significantly impacts electroluminescence (EL) performance in OLEDs and warrants careful consideration during device design. To evaluate the hole transport capabilities of the synthesized compounds, we fabricated single-carrier devices and conducted space-charge-limited current (SCLC) measurements.[85] The architecture of the hole-only devices (HOD) was set to ITO (120 nm)/$MoO_3$ (5 nm)/TAPC (10 nm)/**BCzPh** (150 nm)/$MoO_3$ (10 nm)/Al (120 nm). Here, $MoO_3$ functions as the hole injection and electron blocking layer, while TAPC served as the hole transport layer. The electron-only devices (EOD) adopted the following architecture: ITO (120 nm)/CN-T2T (10 nm)/**BCzPh** (150 nm)/CN-T2T (10 nm)/CN-T2T:$Li_2CO_3$ 10 wt% (5 nm)/Al (120 nm), where CN-T2T and CN-T2T:$Li_2CO_3$ acted as the hole blocking layer and the electron transport/injection layer, respectively.

Fig. 7(a) displays the *J*–*V* curves for the hole-only devices incorporating the synthesized **BCzPh**-based compounds. Given

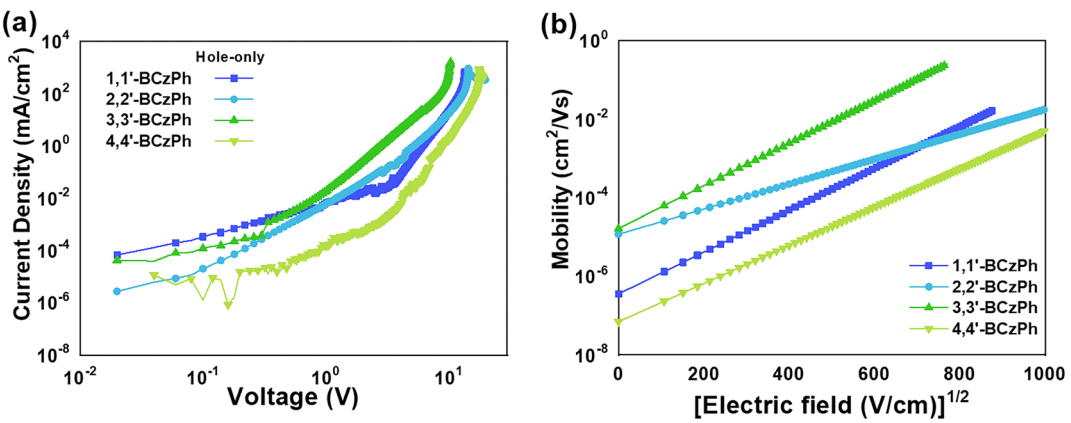


Fig. 7 (a) Current density–voltage (*J*–*V*) curves of the hole-only devices and (b) comparative field dependence mobility of **BCzPh**-based compounds.

the comparable HOMO/LUMO energy levels of the target compounds, the outcome of the current density primarily reflects their charge transport capabilities. For the hole-only devices, the current density follows the trend **3,3′-BCzPh** > **2,2′-BCzPh** > **1,1′-BCzPh** > **4,4′-BCzPh**. In sharp contrast, the electron-only devices presented ultra-low current density values, indicating that these compounds could primarily transport holes. Hole mobilities were calculated based on the SCLC theory, presuming the evaporated organic solid films possess an inherently disordered morphology. The corresponding formula for carrier mobility is provided in the ESI† (page S28). A comparison of field-dependent hole mobility among the **BCzPh**-based compounds is illustrated in Fig. 7(b). The trend in hole mobility values at a field of 0.25 MV $cm^{-1}$ mirrored the current density trend, with values of ($\mu$(**1,1′-BCzPh**) = 1.6 × $10^{-4}$ $cm^2$ $V^{-1}$ $s^{-1}$, $\mu$(**2,2′-BCzPh**) = 4.6 × $10^{-4}$ $cm^2$ $V^{-1}$ $s^{-1}$, $\mu$(**3,3′-BCzPh**) = 8.5 × $10^{-3}$ $cm^2$ $V^{-1}$ $s^{-1}$, and $\mu$(**4,4′-BCzPh**) = 1.9 × $10^{-5}$ $cm^2$ $V^{-1}$ $s^{-1}$). The hole mobility values of the first three compounds are comparable to those of commonly used hole transport materials,[86,87] enabling efficient hole injection from the HTL to the emitting layer (EML) without significant deceleration. The connectivity and twist angle variation in the **BCzPh** series significantly alter the electronic communication, as revealed by the correlatable trends in current density/hole-mobility. These results, in alignment with the X-ray packing arrangement, suggest that well-designed devices, combined with this new set of **BCz**-based synthetic compounds, can achieve satisfactory electroluminescent (EL) performance.

To further understand the carrier transport capabilities of the EML, we fabricated HOD and EOD using the synthesized compounds blended with B3PyMPM in a 1 : 1 ratio, as shown in Fig. 8. The hole transport properties of the blended samples closely mirrored those of the pure synthesized compounds (*cf.* Fig. 7 and 8(a), (b)). The current density in the blended hole-only devices followed the trend **3,3′-BCzPh** > **2,2′-BCzPh** > **1,1′-BCzPh** > **4,4′-BCzPh**. This trend was also reflected in hole mobility values at an electric field of 0.25 MV $cm^{-1}$, with values of ($\mu$(**1,1′-BCzPh**) = 2.3 × $10^{-6}$ $cm^2$ $V^{-1}$ $s^{-1}$, $\mu$(**2,2′-BCzPh**) = 5.4 × $10^{-6}$ $cm^2$ $V^{-1}$ $s^{-1}$, $\mu$(**3,3′-BCzPh**) = 2.2 × $10^{-4}$ $cm^2$ $V^{-1}$ $s^{-1}$, and $\mu$(**4,4′-BCzPh**) = 1.7 × $10^{-6}$ $cm^2$ $V^{-1}$ $s^{-1}$). Interestingly, the hole mobility values for the blended hole-only devices were lower than those of pure hole-only devices, suggesting that the addition of B3PyMPM influences the morphology of the EML, thereby reducing hole transport capabilities. In sharp contrast, the current density of the blended electron-only devices was significantly higher than that of the pure electron-only devices (Fig. 8(c) and (d)), demonstrating the enhanced electron transport ability achieved by incorporating the electron transport material into the EML. The current density in the blended

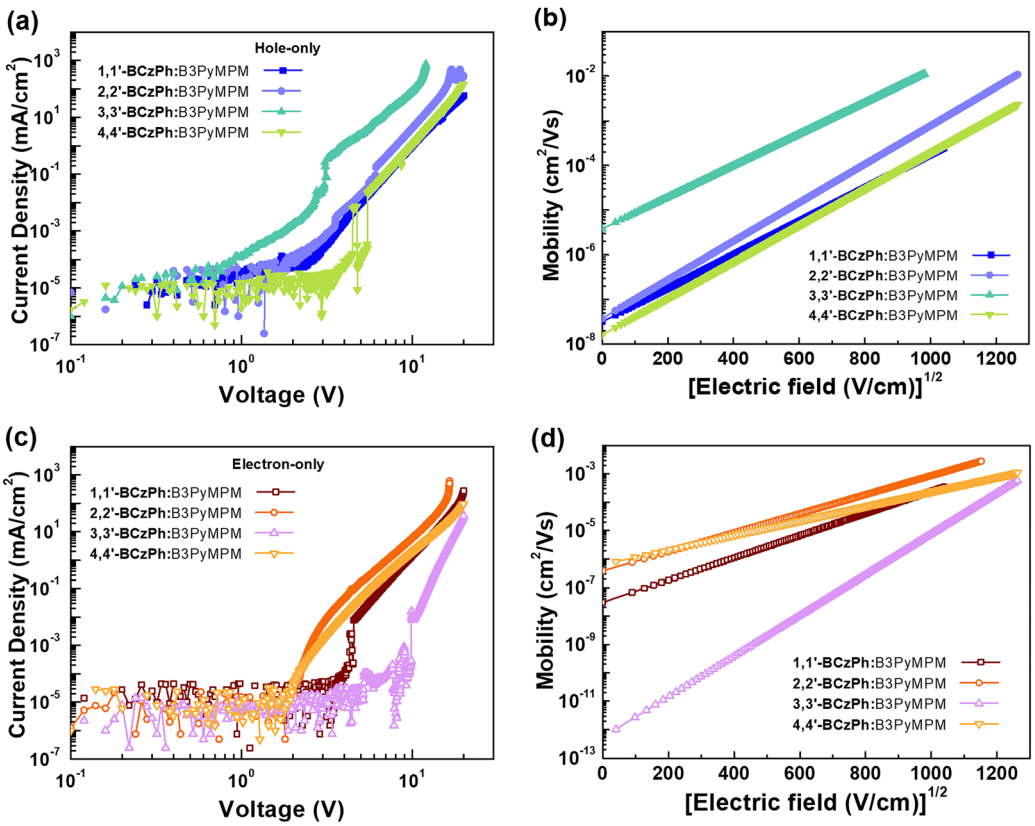


Fig. 8 (a) Current density–voltage (*J*–*V*) curves of the hole-only devices; (b) comparative field dependence hole mobility of **BCzPh**:B3PyMPM-based samples; (c) current density–voltage (*J*–*V*) curves of the electron-only devices; (d) comparative field dependence electron mobility of **BCzPh**:B3PyMPM-based samples.

electron-only devices followed the trend **2,2′-BCzPh** > **4,4′-BCzPh** > **1,1′-BCzPh** > **3,3′-BCzPh**, which was consistent with the electron mobility values at a field of 0.25 MV $cm^{-1}$: ($\mu$(**1,1′-BCzPh**) = 2.7 × $10^{-6}$ $cm^2$ $V^{-1}$ $s^{-1}$, $\mu$(**2,2′-BCzPh**) = 1.8 × $10^{-5}$ $cm^2$ $V^{-1}$ $s^{-1}$, $\mu$(**3,3′-BCzPh**) = 2.0 × $10^{-9}$ $cm^2$ $V^{-1}$ $s^{-1}$, and $\mu$(**4,4′-BCzPh**) = 1.2 × $10^{-5}$ $cm^2$ $V^{-1}$ $s^{-1}$). Notably, the reported electron mobility of B3PyMPM is *ca.* 1.5 × $10^{-5}$ $cm^2$ $V^{-1}$ $s^{-1}$, which aligns closely with the electron mobility of the blended devices, except for the **4,4′-BCzPh** case. Clearly, the electron transport capability of the blended sample was significantly mitigated by **4,4′-BCzPh**. Overall, these results indicate that the blended samples function as bipolar host systems, enabling easier-to-achieve carrier balance in the devices, improving their overall performance.

### 2.8. OLED device performance

To evaluate the performance of bicarbazole-based host materials in the EL devices, we incorporated the highly efficient green-emitting Ir(ppy)$_3$ ($E_T$ = 2.4 eV) as the emitter. The selected **BCzPh** compounds possess only hole transport capabilities. Therefore, we designed an EML using a co-host system that blends two materials with complementary carrier transport properties. For the electron transport part of the EML, we chose B3PyMPM, a material with a wide triplet energy band gap and suitable electron transport capability. We constructed the EML of the devices by including the synthesized compounds and B3PyMPM in a 1 : 1 (wt/wt) blending ratio. Furthermore, the HOMO energy levels of the synthesized **BCzPh** compounds align closely with those of 1,1-bis[(di-4-tolylamino)phenyl]-cyclohexane (TAPC), thus obviating the need for a conventional step-wise HTL design in green-emitting devices.[88] The energy barrier at the interface between HTL and EML is minimal, facilitating hole injection into the EML. On the electron transport side, to address the energy barrier between ETL and EML, B3PyMPM was selected for the ETL, positioned between the EML and the lithium fluoride (LiF)-electron injection layer (EIL). This straightforward configuration enables effective exciton confinement and efficient carrier transport within the device. Furthermore, considering the slightly different carrier transport capabilities and energy gaps of the target compounds, we carefully adjusted the device architectures and the thicknesses of each layer to optimize EL efficiency. Consequently, the green-emitting OLEDs were fabricated using the following architecture: indium tin oxide (ITO) (120 nm)/TAPC (30 nm)/host doped with 8 wt% Ir(ppy)$_3$ (25 nm)/B3PyMPM (50 nm)/LiF (1.5 nm)/Al (150 nm), with ITO and aluminum, functioning as the anode and cathode, respectively. The host materials in the EML were assigned as follows: **1,1′-BCzPh** : B3PyMPM (1 : 1) for Device A, **2,2′-BCzPh** : B3PyMPM (1 : 1) for Device B, **3,3′-BCzPh** : B3PyMPM (1 : 1) for Device C, and **4,4′-BCzPh** : B3PyMPM (1 : 1) for Device D. Fig. 9 provides the materials used, schematic architectures, and energy level diagrams of the fabricated green-emitting OLEDs.

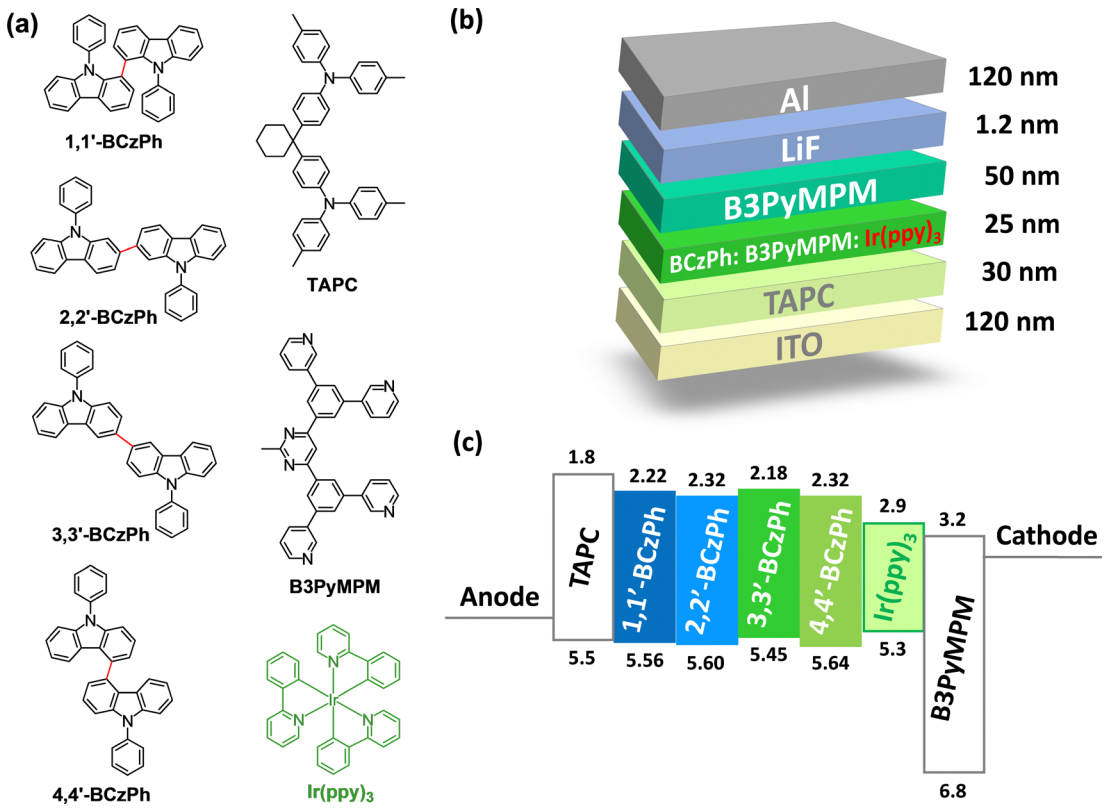


Fig. 9 (a) Schematic illustration of materials used in OLEDs; (b) schematic illustration of green phosphorescent OLED device structures with different host systems; (c) energy level alignment diagram of the used materials.

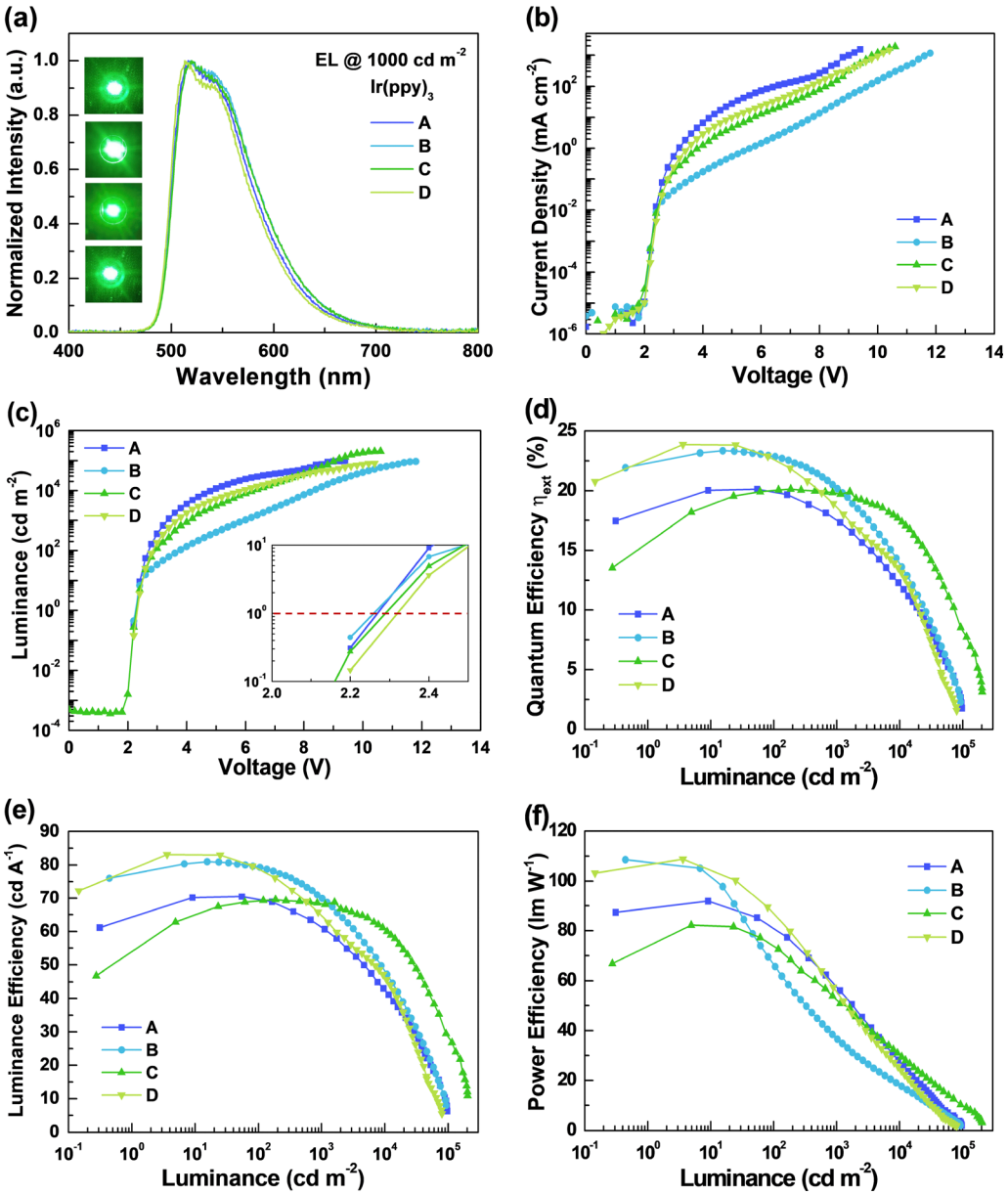


Fig. 10 (a) Normalized EL spectra at a luminance of 1000 cd $m^{-2}$; (b) current density–voltage (*J*–*V*) characteristics; (c) luminance–voltage (*L*–*V*) characteristics; (d) external quantum efficiency (EQE) *vs.* luminance plot; (e) luminance efficiency *vs.* luminance plot; (f) power efficiency *vs.* luminance plot for devices A, B, C, and D. (The blended ratio of the co-host is **BCzPh** : B3PyMPM = 1 : 1.)

Fig. 10 presents the EL characteristics of the devices, and Table 3 provides the corresponding numerical data. As shown in Fig. 10(a), the EL spectra of all devices, recorded at a luminance of 1000 cd $m^{-2}$, exhibit pure $Ir(ppy)_3$ emission. No emissions from the host or the carrier transport materials were detected, implying efficient energy transfer from the co-host to the guest in each green-emitting device, as well as effective exciton confinement within the EML.[89] Moreover, variations in optical path differences among the examined devices arose from the diverse positions of exciton formation regions within the EML, leading to minor discrepancies in the spectral profiles that occur in the longer wavelength regions.[90] Fig. 10(b) presents the current density–voltage (*J*–*V*) curves for the devices. The current density of devices follows the trend A > D > C > B. For example, at an operating voltage of 6 V, the respective current density values for devices A, B, C, and D are 73.0, 1.5, 12.8, and 23.4 mA $cm^{-2}$, respectively. This trend is inconsistent from the behavior observed in the blended carrier-only devices discussed earlier. Device A, employing a **1,1′-BCzPh**:B3PyMPM EML, demonstrated the most balanced carrier transport mobility, favoring a balanced charge transport condition and minimizing the number of trapped carriers within the EML. However, the current densities of the other devices did not directly align with the carrier mobility results, likely due to the influence of additional emissive dopants within the EML. The luminance–voltage (*L*–*V*) characteristics

Table 3 EL characteristics of $Ir(ppy)_3$-based OLEDs with different EML systems

| Device | | A | B | C | D |
|---|---|---|---|---|---|
| **BCzPh** : B3PyMPM (1 : 1) | | **1,1′-BCzPh** | **2,2′-BCzPh** | **3,3′-BCzPh** | **4,4′-BCzPh** |
| External quantum efficiency (%) | [a] | 20.1 | 23.4 | 20.1 | 23.9 |
| | [b] | 19.9 | 22.9 | 20.0 | 22.7 |
| Luminance efficiency (cd $A^{-1}$) | [a] | 70.5 | 81.0 | 69.6 | 83.1 |
| | [b] | 69.8 | 79.4 | 69.1 | 79.0 |
| Power efficiency (lm $W^{-1}$) | [a] | 91.9 | 108.6 | 82.1 | 108.8 |
| | [b] | 81.9 | 66.5 | 74.1 | 87.6 |
| $V_{on}$ (V) | [c] | 2.22 | 2.22 | 2.23 | 2.25 |
| $\lambda_{max}$ (nm) | [d] | 516.5 | 519.0 | 520.0 | 513.0 |
| Max. luminance (cd $m^{-2}$) [V] | | 96 953 [9.4] | 92 593 [11.8] | 203 494 [10.6] | 80 158 [10.4] |
| CIE 1931 coordinates ($x$,$y$) | [b] | (0.34, 0.60) | (0.36, 0.60) | (0.35, 0.60) | (0.34, 0.61) |
| | [d] | (0.34, 0.60) | (0.35, 0.60) | (0.35, 0.60) | (0.33, 0.61) |

[a] Maximum efficiency. [b] Recorded at $10^2$ cd $m^{-2}$. [c] Turn-on voltage measurement at 1 cd $m^{-2}$. [d] Recorded at $10^3$ cd $m^{-2}$.

of the devices are depicted in Fig. 10(c). All tested devices exhibited a low turn-on voltage of approximately 2.2–2.3 V. A similar turn-on voltage may be attributed to the combined effects of current density and efficiency across the devices. Notably, device C, featuring **3,3′-BCzPh**, achieved an impressive maximum luminance exceeding 200 000 cd $m^{-2}$, highlighting its potential for diverse practical applications.

Fig. 10(d)–(f) respectively show the external quantum efficiency, luminance efficiency, and power efficiency *versus* luminance for the tested devices (A–D). The corresponding maximum efficiencies of devices A, B, C, and D reached 20.1% (70.5 cd $A^{-1}$ and 91.9 lm $W^{-1}$), 23.4% (81.0 cd $A^{-1}$ and 108.6 lm $W^{-1}$), 20.1% (69.6 cd $A^{-1}$ and 82.1 lm $W^{-1}$), and 23.9% (83.1 cd $A^{-1}$ and 108.8 lm $W^{-1}$). Essentially, devices using host materials based on **BCzPh** demonstrated a maximum efficiency surpassing 20% (Table 3), suggesting the ease of achieving carrier balance despite differing carrier transport capabilities. Devices B and D, in particular, exhibited superior efficiency, indicating that both **2,2′-BCzPh** and **4,4′-BCzPh** with B3PyMPM effectively create superior carrier balance conditions in the EML. At a higher practical luminance of 100 cd $m^{-2}$, the efficiency of device B remained at 22.9% (79.4 cd $A^{-1}$ and 66.5 lm $W^{-1}$), while device D sustained an efficiency of 22.7% (79.0 cd $A^{-1}$ and 87.6 lm $W^{-1}$). Thus, the EQE values of devices B and D showed efficiency drops of 2.1% and 5.0% from their respective peak values compared to those recorded at 100 cd $m^{-2}$. This indicates that the mitigated efficiency roll-off can be attributed to the extended exciton formation zone and stable carrier balance in these co-host systems, which minimize triplet–triplet annihilation (TTA).[91] In general, incorporating **2,2′-BCzPh** and **4,4′-BCzPh** (devices B and D, respectively) with B3PyMPM as the co-host EML yielded strong EL performance, underscoring the effectiveness of our molecular structure and device designs for achieving efficient green PhOLEDs. It is important to note that **2,2′-BCzPh**, **1,1′-BCzPh**, and **4,4′-BCzPh** have not been investigated as hosts in green PhOLEDs, in contrast to the well-known **3,3′-BCzPh**. The performance observed here for regioisomeric **BCzPh**-based unipolar host materials are exemplary when compared to those already reported (see Table S10 for comparison, page S31, ESI†). For instance, the hosts **3,3′-BCzPh** and ***m*CP** with dopant emitter FIrpic produced blue-light emission with maximum external efficiencies of 16.4 and 13.8%, respectively.[63] Pure-hydrocarbon hosts **1,1′-(SBF)$_2$** and **3,3′-(SBF)$_2$** with FIrpic emitter yielded blue emitting PhOLED with external quantum efficiencies 20.1% and 11.4%, respectively.[9,92,93] Bipolar host material **CBP** with $Ir(ppy)_3$ and **BCz**s with $Ir(ppy)_2(acac)$, resulted in green emission with external quantum efficiencies 17.10%[81] and 14.6–16.8%,[70] respectively. Correlating the twist angle with electronic, carrier transport and device performance characteristics (Fig. S12, ESI†) clearly reveals that the extended π-conjugation in **3,3′-BCzPh** contributes to improved hole mobility and outstanding luminance. Meanwhile, connectivity- or steric-inhibited resonance in **2,2′-BCzPh** and **4,4′-BCzPh** yield excellent luminance, power, and external quantum efficiencies. If one looks at higher brightness levels of 5000 cd $m^{-2}$, the efficiency roll-off behavior showed a difference. The efficiency roll-off values evaluated from the peak to the luminance of 5000 cd $m^{-2}$ are as follows: 29.9% for device A, 28.1% for device B, 7.5% for device C, and 36.9% for device D. The significantly reduced efficiency roll-off for device C (with **3,3′-BCzPh**) illustrates the advantage of balanced carrier transport, relaxing exciton quenching. The notably higher maximum luminance in device C further demonstrates superior carrier transport capabilities of **3,3′-BCzPh**. This design insight is crucial for developing successful next-generation molecular materials.

## 3. Conclusions

In conclusion, we successfully synthesized regioisomeric bicarbazoles (**BCzPh**s) with varying degrees of twist using oxidative/transition-metal catalyzed Suzuki coupling methods. The connectivity differences between the isomers imparted significant structural modifications that can be correlated to variations in photophysical, thermal, and electrochemical properties, as well as in device performance data. Resonance and conjugation effects operate in BCzs mutually contribute to altering the triplet energy levels. Notably, increasing the twist angle between the carbazole planes resulted in larger

singlet–triplet/HOMO–LUMO energy gaps, leading to improved power and luminance efficiencies. Despite these differences, external quantum efficiencies were comparable across devices (A and C, and B and D), with devices B and D with **BCzPh** having *meta–meta* nitrogens realizing outstanding external quantum efficiencies up to 23.9%. Device C exhibited exceptional maximum brightness, followed closely by device A, both with **BCzPh** having *para–para* nitrogens. These results suggest that connectivity differences play a pivotal role in determining device performance. All **BCzPh** compounds demonstrated excellent performance as host materials, delivering stable, high-purity green emission in devices that turned on at voltages as low as 2.2–2.3 V.

## 4. Experimental section

All detailed experimental procedures for the synthesis, OLED device fabrication and characterization of this work are in the ESI.†

## Data availability

The data (detailed synthetic procedure and characterization, structural characterization details, theoretical calculations, spectroscopic, electrochemical and thermal, and device fabrication and performance details) supporting this article is available in ESI.† Crystallographic data for **1,1′-BCzPh** (CCDC no. 2361782), **2,2′-BCzPh** (CCDC no. 2361784), and **4,4′-BCzPh** (CCDC no. 2361783) can be obtained from ESI.†

## Conflicts of interest

There are no conflicts of interest to declare.

## Acknowledgements

PVK gratefully acknowledges IIT Madras for the generous funding support through IoE-EC-ACESC (SP22231245CPMOEXEGYHOC), Ministry of Education, Government of India. KK and SM wishes to thank IIT Madras for a senior research fellowship (SRF). We thank Department of Chemistry, Indian Institute of Technology Madras for the infrastructural facility. This work was financially supported by the National Science and Technology Council of Taiwan (NSTC 111-2221-E-155-012-MY2, NSTC 112-2923-E-155-002-MY4, NSTC 112-2113-M-029-004, NSTC 113-2113-M-029-001, and NSTC 113-2113-M-001-005). Institute of Chemistry, Academia Sinica, Yuan Ze University and Tunghai University are gratefully acknowledged.

## References

1 C. Adachi, M. A. Baldo, M. E. Thompson and S. R. Forrest, *J. Appl. Phys.*, 2001, **90**, 5048–5051.
2 Q. Wang, J. Ding, D. Ma, Y. Cheng, L. Wang, X. Jing and F. Wang, *Adv. Funct. Mater.*, 2009, **19**, 84–95.
3 L. Xiao, Z. Chen, B. Qu, J. Luo, S. Kong, Q. Gong and J. Kido, *Adv. Mater.*, 2011, **23**, 926–952.
4 D. Blazevicius and S. Grigalevicius, *Nanomaterials*, 2024, **14**, 356.
5 G. Fan and D. Yan, *Sci. Rep.*, 2014, **4**, 1–8.
6 C. Poriel and J. Rault-Berthelot, *Acc. Chem. Res.*, 2018, **51**, 1818–1830.
7 C. Poriel, L. Sicard and J. Rault-Berthelot, *Chem. Commun.*, 2019, **55**, 14238–14254.
8 P. Ledwon, *Org. Electron.*, 2019, **75**, 105422.
9 C. Poriel, C. Quinton, F. Lucas, J. Rault-Berthelot, Z.-Q. Jiang and O. Jeannin, *Adv. Funct. Mater.*, 2021, **31**, 2104980.
10 Y. Xiong, J. Gong, J. Liu, D. Wang, H. Wu, Z. Zhao, M. Fang, Z. Li, D. Wang and B. Z. Tang, *J. Mater. Chem. C*, 2022, **10**, 10009–10016.
11 G. Yuan, Y. Z. Yang, D. H. Wang, F. M. Xie, Q. Zhang, Y. Q. Li, Y. Y. Hu, J. X. Tang and X. Zhao, *Dyes Pigm.*, 2024, **224**, 111981.
12 Z. Wu, Z. Xu, D. Wang, G. Deng, S. Lin, Z. Zhao, D. Wang, Y. Xiong and B. Z. Tang, *Adv. Funct. Mater.*, 2025, **35**, 2415285.
13 D. Thakur, M. R. Nagar, A. Tomar, D. K. Dubey, S. Kumar, S. S. Swayamprabha, S. Banik, J. H. Jou and S. Ghosh, *ACS Appl. Electron. Mater.*, 2021, **3**, 2317–2332.
14 C. Brouillac, J. Rault-Berthelot, C. Quinton, C. Poriel, F.-C. Kong and Z.-Q. Jiang, *Adv. Mater. Technol.*, 2023, **8**, 2300763.
15 R. Wang, Y. Zhu, D. Hu, J. Hu, S. Wei Chen, J. Lin, L. Xing, Y. Huo and S. Ji, *Chem. Eng. J.*, 2025, **506**, 160269.
16 M. Chen, Y. Chen, T. Zhang, H. Zhang, Z. Xiao, Z. Su and Y. Wu, *RSC Adv.*, 2024, **14**, 32221–32228.
17 Y. Liu, J. Yang, Z. Mao, Y. Wang, J. Zhao, S.-J. Su and Z. Chi, *Chem. Sci.*, 2023, **14**, 1551–1556.
18 A. A. Sutanto, V. Joseph, C. Igci, O. A. Syzgantseva, M. A. Syzgantseva, V. Jankauskas, K. Rakstys, V. I. E. Queloz, P.-Y. Huang, J.-S. Ni, S. Kinge, A. M. Asiri, M.-C. Chen and M. K. Nazeeruddin, *Chem. Mater.*, 2021, **33**, 3286–3296.
19 X. Zhang, T. Xu, Z. Tian, X. He, S. Zhang, L. Ai, W. Zhang, S. Liu and W. Song, *Chem. Commun.*, 2023, **59**, 5874–5877.
20 J. W. Chung, Y. You, H. S. Huh, B.-K. An, S.-J. Yoon, S. H. Kim, S. W. Lee and S. Y. Park, *J. Am. Chem. Soc.*, 2009, **131**(23), 8163–8172.
21 G. Fan and D. Yan, *Sci. Rep.*, 2014, **4**, 4933.
22 A. V. Monika, M. K. Tiwari, B. Show and S. Saha, *ACS Omega*, 2020, **5**, 448.
23 H. Yi, X. Qin, L. Zhai, H. Duan, H. Chen, Y. Zuo, X. Lian, K. Tian, J. Zhang, Z. Liu and P. Xu, *Precis. Chem.*, 2023, **1**, 548–554.
24 Y. Xiong, Z. Zhao, W. Zhao, H. Ma, Q. Peng, Z. He, X. Zhang, Y. Chen, X. He, J. W. Y. Lam and B. Z. Tang, *Angew. Chem., Int. Ed.*, 2018, **57**, 7997–8001.
25 C. Chen, Z. Chi, K. C. Chong, A. S. Batsanov, Z. Yang, Z. Mao, Z. Yang and B. Liu, *Nat. Mater.*, 2021, **20**, 175–180.
26 K. Zheng, X. Yang, F. Ni, Z. Chen, C. Zhong and C. Yang, *Chem. Eng. J.*, 2021, **408**, 12730.

27 R. Wang, C. Wu, J. Qi, W. Shen, F. Wu, M. Li, R. He, X. Liu, R. Wang, C. Wu, J. Qi, W. Shen, M. Li, R. He, X. Liu and F. Wu, *Adv. Funct. Mater.*, 2023, **33**, 2213843.
28 L. Sicard, C. Quinton, J.-D. Peltier, D. Tondelier, B. Geffroy, U. Biapo, R. Métivier, O. Jeannin, J. Rault-Berthelot and C. Poriel, *Chem. – Eur. J.*, 2017, **23**, 7719–7727.
29 C. Poriel and J. Rault-Berthelot, *Chem. Soc. Rev.*, 2023, **52**, 6754–6805.
30 N. Blouin and M. Leclerc, *Acc. Chem. Res.*, 2008, **41**, 1110–1119.
31 Z. Xu, D. Wu, C. Fang and Y. Li, *Des. Monomers Polym.*, 2023, **26**, 90–105.
32 N. Chopra, J. Lee, Y. Zheng, S.-H. Eom, J. Xue and F. So, *ACS Appl. Mater. Interfaces*, 2009, **1**, 1169–1172.
33 S. O. Jeon, K. S. Yook, C. W. Joo and J. Y. Lee, *Adv. Mater.*, 2010, **22**, 1872–1876.
34 S. J. Lee, J. S. Park, K.-J. Yoon, Y.-I. Kim, S.-H. Jin, S. K. Kang, Y.-S. Gal, S. Kang, J. Y. Lee, J.-W. Kang, S.-H. Lee, H.-D. Park and J.-J. Kim, *Adv. Funct. Mater.*, 2008, **18**, 3922–3930.
35 Y. J. Cho, K. S. Yook and J. Y. Lee, *Adv. Mater.*, 2014, **26**, 4050–4055.
36 M. H. Tsai, H. W. Lin, H. C. Su, T. H. Ke, C. C. Wu, F. C. Fang, Y. L. Liao, K. T. Wong and C. I. Wu, *Adv. Mater.*, 2006, **18**, 1216–1220.
37 R. J. Holmes, S. R. Forrest, Y. J. Tung, R. C. Kwong, J. J. Brown, S. Garon and M. E. Thompson, *Appl. Phys. Lett.*, 2003, **82**, 2422–2424.
38 K. L. Woon, Z. A. Hasan, B. K. Ong, A. Ariffin, R. Griniene, S. Grigalevicius and S.-A. Chen, *RSC Adv.*, 2015, **5**, 59960–59969.
39 K. S. Yook and J. Y. Lee, *Adv. Mater.*, 2012, **24**, 3169–3190.
40 N. Thejo Kalyani and S. J. Dhoble, *Renewable Sustainable Energy Rev.*, 2015, **44**, 319–347.
41 Y. Wang, J. H. Yun, L. Wang and J. Y. Lee, *Adv. Funct. Mater.*, 2021, **31**, 2008332.
42 S. Oner and M. R. Bryce, *Mater. Chem. Front.*, 2023, **7**, 4304–4338.
43 S. Kasemthaveechok, L. Abella, M. Jean, M. Cordier, N. Vanthuyne, T. Guizouarn, O. Cador, J. Autschbach, J. Crassous and L. Favereau, *J. Am. Chem. Soc.*, 2022, **144**, 7253–7263.
44 G. Krucaite and S. Grigalevicius, *Synth. Met.*, 2019, **247**, 90–108.
45 K. Brunner, A. van Dijken, H. Börner, J. J. A. M. Bastiaansen, N. M. M. Kiggen and B. M. W. Langeveld, *J. Am. Chem. Soc.*, 2004, **126**, 6035–6042.
46 D. Li, J. Li, D. Liu, W. Li, C.-L. Ko, W.-Y. Hung and C. Duan, *ACS Appl. Mater. Interfaces*, 2021, **13**, 13459–13469.
47 S.-i Kato, H. Noguchi, A. Kobayashi, T. Yoshihara, S. Tobita and Y. Nakamura, *J. Org. Chem.*, 2012, **77**, 9120–9133.
48 C. Jiang, X. Huang, B. Sun, Y. Li, M. Gao, L. Ye, H. Ade, S. R. Forrest and J. Fan, *Org. Electron.*, 2020, **84**, 105784.
49 S.-O. Jeon, K. S. Yook, C. W. Joo, J. Y. Lee, K.-Y. Ko, J.-Y. Park and Y. G. Baek, *Appl. Phys. Lett.*, 2008, **93**, 063306.
50 M. A. Baldo, S. Lamansky, P. E. Burrows, M. E. Thompson and S. R. Forrest, *Appl. Phys. Lett.*, 1999, **75**, 4–6.
51 M. A. Baldo and S. R. Forrest, *Phys. Rev. B: Condens. Matter Mater. Phys.*, 2000, **62**, 10958–10966.
52 C. Adachi, R. C. Kwong, P. Djurovich, V. Adamovich, M. A. Baldo, M. E. Thompson and S. R. Forrest, *Appl. Phys. Lett.*, 2001, **79**, 2082–2084.
53 H. Mu, Y. Jiang and H. Xie, *Org. Electron.*, 2019, **66**, 195–205.
54 Y. H. Jeong, C. W. Joo, H. Jeong, J. Lee and Y.-H. Kim, *J. Inf. Disp.*, 2022, **23**, 273–279.
55 D. Sun, X. Zhou, J. Liu, X. Sun, H. Li, Z. Ren, D. Ma, M. R. Bryce and S. Yan, *ACS Appl. Mater. Interfaces*, 2015, **7**, 27989–27998.
56 W. Jiang, L. Duan, J. Qiao, D. Zhang, G. Dong, L. Wang and Y. Qiu, *J. Mater. Chem.*, 2010, **20**, 6131–6137.
57 J. S. Swensen, E. Polikarpov, A. Von Ruden, L. Wang, L. S. Sapochak and A. B. Padmaperuma, *Adv. Funct. Mater.*, 2011, **21**, 3250–3258.
58 T. Tsuboi, H. Murayama, S.-J. Yeh, M.-F. Wu and C.-T. Chen, *Opt. Mater.*, 2008, **31**, 366–371.
59 F.-M. Hsu, C.-H. Chien, P.-I. Shih and C.-F. Shu, *Chem. Mater.*, 2009, **21**, 1017–1022.
60 C.-H. Chang, Z.-J. Wu, C.-H. Chiu, Y.-H. Liang, Y.-S. Tsai, J.-L. Liao, Y. Chi, H.-Y. Hsieh, T.-Y. Kuo, G.-H. Lee, H.-A. Pan, P.-T. Chou, J.-S. Lin and M.-R. Tseng, *ACS Appl. Mater. Interfaces*, 2013, **5**, 7341–7351.
61 O. Bezvikonnyi, G. Grybauskaite-Kaminskiene, D. Volyniuk, J. Simokaitiene, Y. Danyliv, R. Durgaryan, A. Bucinskas, E. Jatautienė, I. Hladka, J. Scholz, H. Starykov and J. V. Grazulevicius, *Mater. Sci. Eng., B*, 2020, **261**, 114662.
62 M. Kim and J. Y. Lee, *ACS Appl. Mater. Interfaces*, 2014, **6**, 14874–14880.
63 H. Sasabe, N. Toyota, H. Nakanishi, T. Ishizaka, Y.-J. Pu and J. Kido, *Adv. Mater.*, 2012, **24**, 3212–3217.
64 L.-S. Cui, Y. Liu, X.-D. Yuan, Q. Li, Z.-Q. Jiang and L.-S. Liao, *J. Mater. Chem. C*, 2013, **1**, 8177–8185.
65 M. Kim and J. Y. Lee, *Org. Electron.*, 2013, **14**, 67–73.
66 S. M. Kim, S. Y. Byeon, S. H. Hwang and J. Y. Lee, *Chem. Commun.*, 2015, **51**, 10672–10675.
67 J. Hwang, J. Yoon, C. Y. Kim, S. Choi, H. Kang, J. Y. Kim, D.-W. Yoon, C. W. Han, S. Park, M. J. Cho and D. H. Choi, *Dyes Pigm.*, 2020, **179**, 108403.
68 H.-G. Jang, B. S. Kim, J. Y. Lee and S.-H. Hwang, *Dalton Trans.*, 2014, **43**, 7712–7715.
69 Y.-J. Na, W. Song, J. Y. Lee and S.-H. Hwang, *Dalton Trans.*, 2015, **44**, 8360–8363.
70 X.-Y. Liu, Y.-L. Zhang, X. Fei, L.-S. Liao and J. Fan, *Chem. – Eur. J.*, 2019, **25**, 4501–4508.
71 D. Zhou, B. Zhang, Z. Yu, Q. Liao and H. Fu, *New J. Chem.*, 2020, **44**, 10472–10478.
72 S. Kang, H. Jung, H. Lee, S. Lee, M. Jung, J. Lee, Y. C. Kim and J. Park, *Dyes Pigm.*, 2018, **156**, 369–378.
73 P. Pandit, T. Nakamura and S. Higashibayashi, *Chem. Lett.*, 2015, **44**, 1336–1338.
74 S. Mallick, S. Maddala, K. Kollimalayan and P. Venkatakrishnan, *J. Org. Chem.*, 2019, **84**, 73–93.
75 S. Maddala, C.-L. Chung, S.-Y. Wang, K. Kollimalayan, H.-L. Hsu, P. Venkatakrishnan, C.-P. Chen and Y. J. Chang, *Chem. Mater.*, 2020, **32**, 127–138.

76 N. Miyaura, K. Yamada and A. Suzuki, *Tetrahedron Lett.*, 1979, **20**, 3437–3440.
77 C.-L. Ho, L.-C. Chi, W.-Y. Hung, W.-J. Chen, Y.-C. Lin, H. Wu, E. Mondal, G.-J. Zhou, K.-T. Wong and W.-Y. Wong, *J. Mater. Chem.*, 2012, **22**, 215–224.
78 J. Yuan, L. Jin, R. Chen, X. Tang, X. Xie, Y. Tang and W. Huang, *New J. Chem.*, 2018, **42**, 14704–14708.
79 W. Li, J. Li, D. Liu, F. Wang and S. Zhang, *J. Mater. Chem. C*, 2015, **3**, 12529–12538.
80 Z. He, C. Wang, J. Zhao, X. Du, H. Yang, P. Zhong, C. Zheng, H. Lin, S. Tao and X. Zhang, *J. Mater. Chem. C*, 2019, **7**, 11806–11812.
81 T. Zhang, Y. Liang, J. Cheng and J. Li, *J. Mater. Chem. C*, 2013, **1**, 757–764.
82 J. He, H. Liu, Y. Dai, X. Ou, J. Wang, S. Tao, X. Zhang, P. Wang and D. Ma, *J. Phys. Chem. C*, 2009, **113**, 6761.
83 M.-H. Tsai, Y.-H. Hong, C.-H. Chang, H.-C. Su, C.-C. Wu, A. Matoliukstyte, J. Simokaitiene, S. Grigalevicius, J. V. Grazulevicius and C.-P. Hsu, *Adv. Mater.*, 2007, **19**, 862.
84 C. Chen, K. C. Chong, Y. Pan, G. Qi, S. Xu and B. Liu, *ACS Mater. Lett.*, 2021, **3**, 1081–1087.
85 Y. H. Lin, W.-H. Lin, Y.-S. Huang, C.-H. Wu, P. Gnanasekaran, Y.-M. Chang, S.-W. Teng, C.-W. Lu, C.-H. Chang and Y. J. Chang, *J. Mater. Chem. C*, 2023, **11**, 3101–3111.
86 S. K. So, S. C. Tse and K. L. Tong, *J. Disp. Technol.*, 2007, **3**, 225–232.
87 S. Grigalevicius, D. Tavgeniene, G. Krucaite, R. Griniene, W.-C. Li, D. Luo and C.-H. Chang, *Dyes Pigm.*, 2018, **152**, 100–104.
88 Y.-J. Lien, T.-C. Lin, C.-C. Yang, Y.-C. Chiang, C.-H. Chang, S.-H. Liu, Y.-T. Chen, G.-H. Lee, P.-T. Chou, C.-W. Lu and Y. Chi, *ACS Appl. Mater. Interfaces*, 2017, **9**, 27090–27101.
89 J.-M. Wang, T.-C. Lee, C.-C. Chung, W.-Y. Chen, S.-Y. Wu, Y.-D. Lin, Y. J. Chang, C.-W. Lu and C.-H. Chang, *Chem. Eng. J.*, 2023, **472**, 145023.
90 C.-W. Lu, C.-C. Tsai, Y.-S. Huang, H.-Y. Chih, W.-C. Li, T.-Y. Chiu and C.-H. Chang, *Dyes Pigm.*, 2019, **163**, 145–152.
91 G. Ganesan, P. Balasubramaniam, J. Lade, K.-H. Wang, K.-W. Chen, A. C. Chaskar and C.-H. Chang, *ACS Appl. Opt. Mater.*, 2023, **1**, 1546–1558.
92 L.-S. Cui, Y.-M. Xie, Y.-K. Wang, C. Zhong, Y.-L. Deng, X.-Y. Liu, Z.-Q. Jiang and L.-S. Liao, *Adv. Mater.*, 2015, **27**, 4213–4217.
93 L. J. Sicard, H.-C. Li, Q. Wang, X.-Y. Liu, O. Jeannin, J. Rault-Berthelot, L.-S. Liao, Z.-Q. Jiang and C. Poriel, *Angew. Chem., Int. Ed.*, 2019, **58**, 3848–3853.